Bulletin of the AAS • Celebrating the Wonder of Science in the Shadow II

Revealing the Dynamics of Atmospheric Gravity Waves: Insights from an Annular Solar Eclipse Event at Artesia Science Center, NM

Oana Vesa[1] Juie Shetye[1] Andrew Denney[2] Marco Martinez[1] Christine Houser[1] Aidan Brealey-Rood[3] Judy Evelyn Silva[1] Shayan Abotalebi[4]

[1]Department of Astronomy, New Mexico State University, MSC 4500, PO BOX 30001 Las Cruces, NM 88003,
[2]Physical Science Laboratory, NMSU, 1050 Stewart St, Las Cruces, NM 88003,
[3]Department of Astronomy, NMSU, Las Cruces, NM 88003,
[4]Physical Science Laboratory, NMSU,1050 Stewart St, Las Cruces, NM 88003

Published on: Mar 18, 2025

DOI: https://doi.org/10.3847/25c2cfeb.5ceea9d5

ABSTRACT

We unveil possibly the first detections of annular-eclipse AGWs and their properties at Artesia Science Centre (ASC), an isolated region in New Mexico. ASC was in the path of the 2023 Annular Eclipse, and experienced maximum annularity for 2 mins 30 secs. We launched radiosondes hourly on 22 flights to record changes in Earth's atmosphere, such as temperature and wind direction. We filtered out first-order perturbations and identified AGWs in wavelet diagrams. We observed 55 AGWs at ASC between 00:00 UTC October 14, 2023, and 22:00 UTC on October 14, 2023, this covered the duration of the annular eclipse, which was from approximately 14:00 UTC to 18:00 UTC. Notably, 17 AGWs were detected during the eclipse between the first and last contact, while the remaining waves were observed under non-eclipse conditions. Our analysis of the wave propagation direction reveals a clear pattern, with waves spreading from the launch sites in various directions. The comparison between eclipse-driven and other AGWs shows no significant differences in energy distribution, propagation direction, amplitude, frequency, or momentum flux, indicating that eclipse events do not notably alter AGW properties. Notably, the horizontal wavelengths of AGWs detected during the eclipse are larger than their vertical wavelengths, suggesting stable atmospheric conditions with predominantly horizontal propagation. The energy characteristics of eclipse-driven AGWs are similar to those driven by other atmospheric phenomena, indicating consistent AGW behavior. Our findings imply that while solar eclipses induce AGWs, their properties are consistent with typical AGW behavior observed in the atmosphere. Further research with extensive data and higher resolution measurements is necessary to fully understand eclipse AGW dynamics and their atmospheric impact.

1. Introduction

Solar eclipses are rare celestial events in which the Moon moves between the Earth and the Sun, temporarily blocking sunlight. These phenomena have intrigued humanity and provided a unique chance to observe various atmospheric processes. Notably, atmospheric gravity waves (AGWs) are a key focus during eclipses, as they play a crucial role in atmospheric dynamics and energy transport within the Earth's atmosphere (Espenak & Anderson, 2007; Pasachoff, 2009).

AGWs are created by the displacement of air parcels due to buoyancy forces and are a fundamental component of the Earth's atmosphere. These waves are often generated by various sources, including weather systems, topographic features, and convective processes. These waves play a crucial role in atmospheric processes, influencing weather patterns, climate systems, and even the dynamics of the ionosphere and thermosphere (Fritts & Alexander, 2003).

There is still a lot of contention if eclipses can create or drive AGWs or if they're different from AGWs present in the region where they're formed (Colligan et al., 2020). Thus, investigation of the presence of AGWs during solar eclipses is particularly significant as eclipse events induce rapid and localized changes in atmospheric

conditions, which are ideal for generating and propagating AGWs (Fritts & Alexander, 2003). Furthermore, AGWs propagate both vertically and horizontally, influencing weather patterns, climate systems, and dynamics of ionosphere and thermosphere (Vadas & Liu, 2009; Holton, 1983).

Recent studies have tried to understand the relationship between solar eclipses and AGWs (Aplin & Harrison, 2003; Zerefos et al., 2007; Colligan et al., 2020). Through ground-based measurements, it has been observed that solar eclipses create temperature, pressure, and wind variations that can result in the formation of AGWs (Zerefos et al., 2007). These variations are primarily due to the abrupt reduction and subsequent restoration of solar radiation as the eclipse progresses (Zerefos et al., 2007). The cooling of the Earth's surface during the eclipse leads to a rapid decrease in temperature, creating a thermal gradient that can generate buoyancy waves in the atmosphere (Liu & Roble, 2002; Goodwin & Hobson, 1978). Additionally, the changes in solar heating affect atmospheric pressure and wind patterns, further contributing to the formation of AGWs (Aplin & Harrison, 2003).

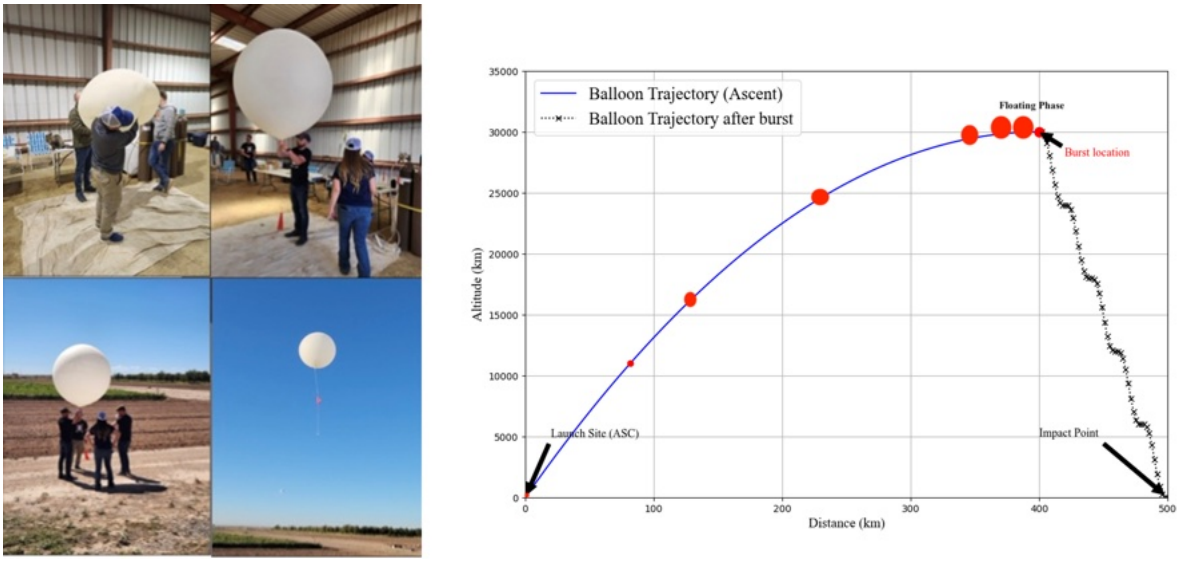

Figure 1

Steps in launching a radiosonde on a high-altitude balloon and its trajectory.

Studies utilizing satellite data and ground-based observations have shown that eclipses can significantly alter wind velocities and induce ionospheric disturbances. For example, during the total solar eclipse of July 2, 2019, radiosonde data collected from field campaigns provided the first direct evidence of AGWs, highlighting significant enhancements in neutral wind velocities and ionospheric disturbances (Colligan et al., 2020). These findings underscore the substantial influence of eclipse-induced gravity waves on upper atmospheric dynamics and serve as a foundation for the current study.

Furthermore, numerically sophisticated simulations have elucidated intricate wave patterns that depend on solar radiation changes and atmospheric conditions (Vadas & Liu, 2009). These simulations reveal that rapid fluctuations in solar radiation can induce temperature gradients, leading to buoyancy-driven oscillations and

the propagation of gravity waves in the atmosphere. Models suggest that the short duration of solar eclipses, usually lasting less than seven minutes, has a significant impact on the generation and propagation of AGWs. However, linking these theoretical models with observational data remains a challenge due to the unique and infrequent nature of solar eclipses (Qiu et al., 2023).

In this manuscript, we present the detections of AGWs observed at Artesia Science Centre (ASC), which experienced maximum annularity for 2 min 30 sec on October 14, 2023, during the annular solar eclipse. We compare the properties of AGWs before, during, and after the eclipse. Our aim was to investigate whether additional AGWs were detected during the eclipse and whether their properties changed during the four hours between the first and last contact.

2. Data and Methods

2.1 Data Collection

In this study, we present data from 22 radiosondes launches that were launched between 00:00 UTC on October 14, 2023, and 22:00 UTC on October 14, 2023, covering the duration of the annular eclipse, which was from approximately 14:00 UTC to 18:00 UTC. To compare with local weather conditions, we conducted three calibration launches between 17:00 UTC and 22:00 UTC on October 13, 2023. The launches were from ASC, which is at the location of 32.75 N, 104.38 W. We collected local atmospheric conditions at ASC to provide a baseline for the data collected as the balloon ascended with the radiosonde on it. The temperature at the launch site was a cool 7.6^{o}C, with a moderately moist humidity level of 64%. The wind direction was measured at 177^{o}, which means the wind was blowing almost directly from the south. The site altitude was a relatively high altitude of 1013 meters above sea level, with an absolute pressure value of 901 hPa (hectopascals), which is slightly lower than the average sea-level pressure of 1013.25 hPa. The tropopause at ASC is expected to be around 13 km.

We launched a radiosonde on a high-altitude balloon using a multi-step process. First, we filled the latex balloon with helium gas, making it buoyant enough to rise through the atmosphere. Then, we attached the radiosonde to the bottom of the balloon with a strong, lightweight string. To ensure a safe descent after the balloon burst, we added a parachute between the balloon and the radiosonde. We then carefully released the balloon from the ground, and as it ascended, it carried the radiosonde upwards through the atmosphere. The balloon rose at a steady rate, typically around 5 meters per second. In our experiments, the balloons typically reached altitudes of 35 kilometers (22 miles) or more. Eventually, the balloon reached a point where the atmospheric pressure decreased so much that it expanded and burst. Throughout its journey, the radiosonde transmitted data on temperature, humidity, pressure, and GPS coordinates. We recorded this data using Grawmet ground stations connected to laptops. In Figure 1, we illustrate the steps we took to launch the radiosonde. The left panel shows photographs from the launch, and the cartoon sketch on the right panel shows the balloon's trajectory.

2.2 Data Processing

We preprocessed the data to remove values below the tropopause and any missing points caused by recording or connection problems. Then, we linearly interpolated the data onto a consistently spaced spatial grid, following the method described by Colligan et al. (2020). We first computed the first-order perturbations within each vertical profile to isolate the influence of atmospheric gravity waves (AGWs). This involved subtracting a second-order polynomial fit from the data, which we obtained using a least squares polynomial fitting method. Once we removed these perturbations, we were able to extract the zonal (east-west) and meridional (north-south) wind components. These components reveal the spatial distribution and movement of air masses impacted by AGW activity.

As AGWs propagate through the atmosphere, they cause oscillations in wind velocity, which in turn lead to changes in wind direction. These waves have characteristic patterns in their wind-direction changes, allowing us to distinguish them from other atmospheric phenomena. Unlike large-scale weather systems or turbulence, which can cause erratic wind direction fluctuations, AGWs produce more organized and coherent changes that align with their own direction of propagation. In the case of AGWs triggered by a solar annular eclipse, these changes occur in the same direction as the eclipse path's movement. The changes also often exhibit periodicity that matches the intrinsic frequency of the AGW, further helping us differentiate AGW signatures from background variations.

2.3 Wavelet analysis:

We use wavelet analysis (Torrence & Compso, 1998) to investigate perturbations in zonal and meridional wind directions and to improve our detections. Individual gravity wave packets can be identified in the vertical wavelength–altitude space from first-order horizontal wind perturbation profiles. Due to the sinusoidal nature of horizontal wind perturbations of gravity waves, which resemble amplitude-modulated sine waves, the Morlet wavelet with a wavenumber of 6 was chosen for the analysis (Zink & Vincent, 2001; Moffat-Griffin et al., 2011). We chose the Morlet wavelet for identifying local maxima because it excels at identifying localized oscillations within data. This wavelet combines a sinusoidal wave with a Gaussian envelope, making it a perfect fit for our needs. We padded the data appropriately before applying the wavelet transform, to minimize edge effects and improve the analysis' accuracy. Our approach utilizes similar scales for the Morlet wavelet transform on the padded data, following the methods outlined by Torrence and Compo (1998). As described by Colligan et al. (2020), the smallest resolvable scale was set to be twice the original spatial resolution of the data. Using the wavelet analysis, we computed wavelet coefficients for the first-order vertical zonal and meridional wind perturbations, defined as $W_u(a,z)$ and $W_v(a,z)$, respectively. Individual gravity wave packets can be located at various scales (a) – in this context, vertical wavelengths – and altitudes (z). Adding the modulus square of the individual wavelet coefficients forms the power surface, defined as:

$$S(a,z)=|W_u(a,z)|^2+|W_v(a,z)|^2$$

We identified local maxima (denoted by red-dot in Figure 2) above a noise threshold of 0.01 m^2/s^2 , and the rectangular boxes show the entire extent of the gravity wave packet (Zink & Vincent, 2001). The cone-of-influence determines regions of errors due to the edge effects of Fourier transforms (Torrence & Compo, 1998). At each local maximum coordinate (a_0,z_0), the rectangular boundary corresponds to where the power surface drops to 0.25 * $S(a_0,z_0)$ or starts rising again. We used the Inverse Wavelet Transform, corresponding to the wind wavelet coefficients defined by this rectangular boundary, to compute *u' and v'*, respectively. These reconstructed variables correspond to potential gravity wave perturbations (Zink & Vincent, 2001). We only considered potential gravity wave packets with vertical extents determined by the full-width half-max of the horizontal wind variance computed from the reconstructed wavelet coefficients (Zink & Vincent, 2001). If the rectangular boundaries of the potential gravity wave packets overlap, then the horizontal wind variance is divided equally between the wave packets to conserve total wind variance (Zink & Vincent, 2001). Figure 2 shows an example of the power surface created from the wavelet analysis indicating possible AGW detections, which are marked by the red dots. We showcase what the boundaries, denoted by the red rectangle, of one gravity wave packet would look like.

We obtained several parameters such as the vertical wavelength λz and vertical wavenumber m of the potential gravity wave packets, the background wind and temperature profiles, and the Brunt-Väisälä frequency N averaged over the vertical extent of the gravity wave packet. The Brunt-Väisälä frequency, which defines the upper frequency bound for gravity wave propagation, was calculated using the mean potential temperature and gravitational acceleration (Moffat-Griffin et al., 2011; Pfenninger et al., 1999).

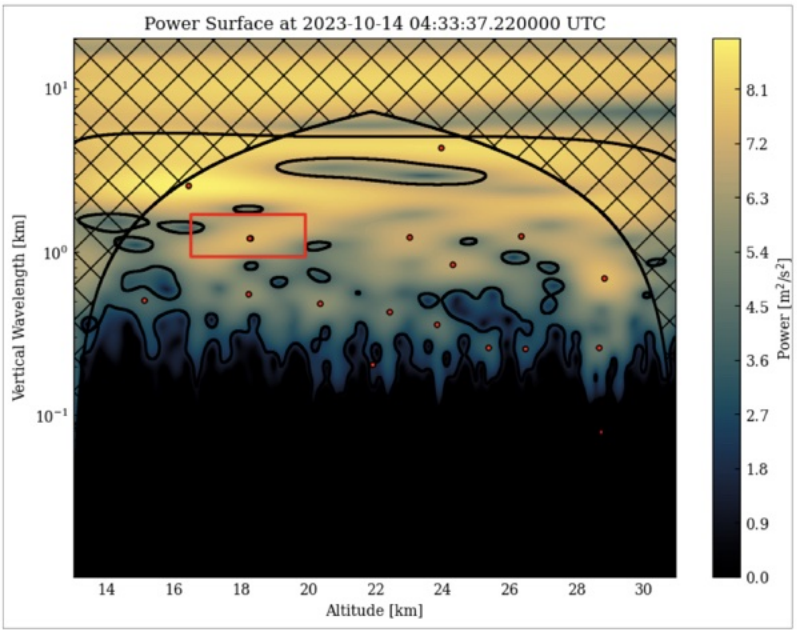

Figure 2
Power surface constructed from wavelet analysis that shows detection of local maxima and the extent of gravity wave packet.

Our analysis used the elliptically polarized nature of AGWs to perform Stokes parameter analysis, a technique commonly used in electromagnetic wave studies. The Stokes parameters (I, Q, U, D) provided valuable insights into the wave packet's polarization, direction of energy propagation, and degree of polarization. They provide information about the intensity (I), the northward (Q) and eastward (U) components of the wave's linear polarization, and the degree of circular polarization (D). Positive Q values specifically indicate that the wave energy is propagating upwards in the Northern Hemisphere, while negative Q values correspond to downward propagation. This follows the established criteria for gravity wave polarization analysis as described by Ren et al. (2023), Murphy et al. (2014), and Koushik et al. (2019). The interpretation of Stokes Q values helps differentiate between upward-propagating AGWs and downward-propagating reflected or secondary waves, providing key insights into wave dynamics and energy transfer in the atmosphere. AGWs must exhibit sufficient polarization, and only those with Stokes P and Stokes Q values greater than 0.05 were retained, as lower values indicate poor wave activity that is unlikely to correspond to a real gravity wave (Koushik et al., 2019). Additionally, the degree of polarization, d, was used as a secondary filter, with $0.5 \leq d < 1$ defining a valid AGW, while values outside this range indicate either a monochromatic wave ($d = 1$) or an invalid detection ($d < 0.5$ or $d > 1$) (Yoo et al., 2020). Lastly, a physical frequency constraint was applied to ensure that each detected wave adhered to fundamental gravity wave propagation limits. According to Murphy et al. (2014), a valid AGW must have an intrinsic frequency greater than the Coriolis frequency but less than the Brunt–Väisälä frequency to propagate in the atmosphere. Detections failing this criterion were automatically excluded from further analysis.

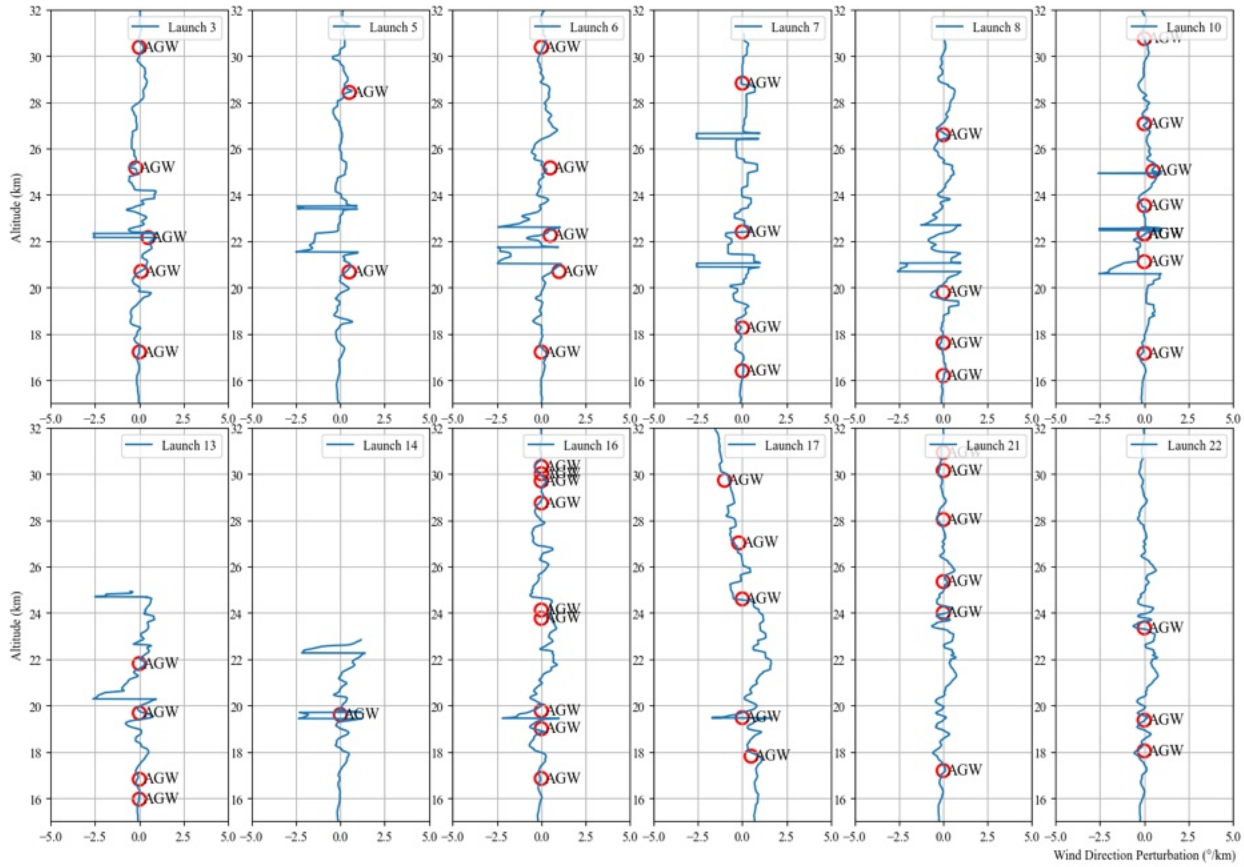

Figure 3

Radiosonde launch trajectories with first order perturbations subtracted. The red circles show location of potential AGWs identified in the Wavelet analysis.

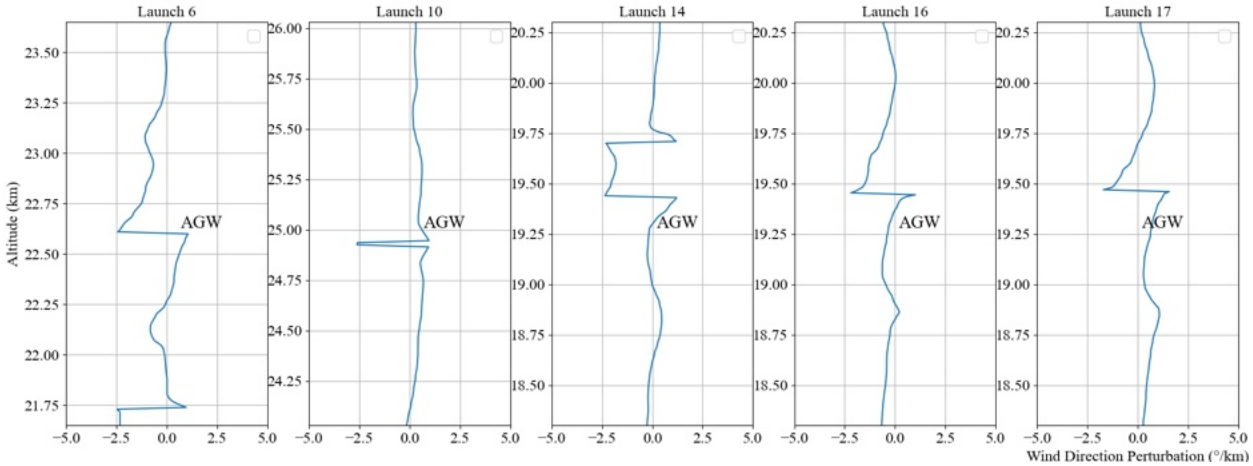

Figure 4

Potential AGWs detected in the wind-direction trajectories for launches 6,10,14,16 and 17.

3. Results and Discussions

The analysis suggests a possible association between the detected atmospheric gravity waves (AGWs) and the annular eclipse. The reconstructed perturbations, derived from the wavelet analysis, provide indications of AGW presence. The red dots in the wavelet spectra highlight regions of strong wave activity, which, when mapped to the radiosonde profiles, often coincide with areas where wind direction changes significantly. This alignment supports our interpretation that these waves are not random fluctuations but may be influenced by eclipse-driven atmospheric changes. However, the connection is not straightforward, and other atmospheric factors could also contribute to the observed patterns.

In Figure 3, we present the radiosonde wind trajectories, where we observe notable perturbations in wind direction at locations where AGWs are detected using the wavelet analysis. To explore this relationship, we overplot the red dots marking AGW maxima in the wavelet spectra as red circles on the radiosonde trajectory plots. These circles indicate locations where AGW-induced directional changes are more pronounced, suggesting a possible link between the detected wave activity and the observed wind fluctuations.

To further investigate these detections, we provide a zoomed-in view in Figure 4 of selected regions from Figure 3, offering additional details on individual wave packets. These focused views allow us to examine how AGW-induced wind fluctuations evolve spatially and temporally. Figure 4 presents wind direction perturbations as a function of altitude for five different radiosonde launches (Launch 6 (before), Launch 10, Launch 14 (during), Launch 16 (during), and Launch 17(during)). Each panel corresponds to a specific launch, showing how the wind direction varies with height. The locations where AGWs are detected are labeled in each panel. The altitude range where AGWs are observed varies across different launches, with notable differences between pre-eclipse and eclipse-period detections. In Launch 6 (before the eclipse), AGW activity is detected between approximately 21.75 km and 23.25 km, while in Launch 10 (before the eclipse), a strong AGW feature appears around 24.75 km. During the eclipse, AGW perturbations are observed at lower altitudes. In Launch 14 (during the eclipse), AGWs are centered at 19.50 km, a pattern that is also seen in Launch 16 (during the eclipse) at 19.50 km. Similarly, Launch 17 (during the eclipse) detects AGW activity at a slightly higher altitude, approximately 19.75 km. These variations suggest a possible influence of the eclipse on AGW activity, as waves observed before the eclipse are at higher altitudes, whereas those detected during the eclipse tend to appear lower in the atmosphere. This shift in altitude may indicate eclipse-driven modifications in atmospheric stability or wave propagation.

In Figure 5, we present the results of the detected AGWs at the ASC. On the left panel, we present the propagation directions of atmospheric gravity waves (AGWs) detected at the ASC. We highlight the umbral shadow path with a yellow band, and the width of the band represents the width of the umbral shadow. Annularity propagation direction is represented in black arrows. We observe that the AGWs propagate in various directions, as indicated by the blue arrows extending from the central launch site. Each arrow represents the direction in which a wave travels, with the arrows radiating outward to illustrate the wave

dispersion across the region. The angles marked around the circumference of the plot help to quantify these directions in degrees. The red arrows highlight the AGWs observed during the duration of the annular eclipse. Note that these waves follow the direction of propagation of annularity.

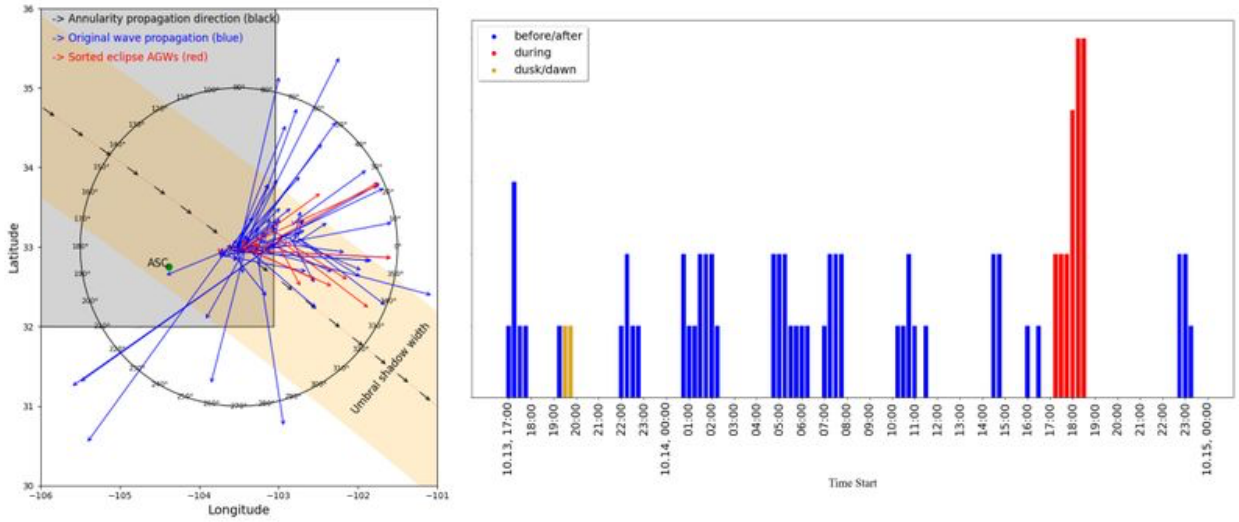

Figure 5
The left panel shows the direction of AGW propagation. Blue arrows indicate AGWs observed between 00:00 UTC and 22:00 UTC on October 14, 2023, while red arrows represent AGWs detected during the eclipse. The length of the arrows is scaled to the horizontal wavelength. The right panel presents the hourly detection of AGWs, where blue bars represent AGWs formed under normal conditions, yellow bars indicate AGWs formed under twilight conditions, and red bars highlight AGWs formed during the eclipse.

The 200 km black circle in the plot serves as a reference frame for the propagation angles, with degrees marked around its circumference. This circle helps us quantify the direction in which each wave travels, making it easier to visualize the dispersion patterns of the waves from the launch site. From the graph, we can see that the wave propagation is not uniform, with certain directions exhibiting more wave activity. This directional distribution may be influenced by local topography, atmospheric conditions, or other environmental factors present at the time of wave detection.

In the right panel of Figure 5, we present the number of detected atmospheric gravity waves (AGWs) throughout the experiment, totaling 55 identified AGWs. The histogram categorizes AGWs based on the time of detection: blue bars represent AGWs detected before and after the eclipse, red bars correspond to AGWs detected during the eclipse, and yellow bars indicate AGWs detected during twilight (dusk/dawn transitions). From the distribution, we observe that AGWs were present at various times throughout the experiment, but there is a notable increase in AGW activity during the eclipse period, as seen in the cluster of red bars between

approximately 16:00 and 20:00 UTC on October 14, 2023. The number of detected AGWs peaks around 18:00 UTC, coinciding with the period when the annular eclipse occurred. Before and after the eclipse, AGWs appear more sporadically, with relatively lower counts per time interval. Additionally, the presence of twilight AGWs (yellow bars) suggests that certain waves could be influenced by diurnal atmospheric transitions, which are known to affect wave generation and propagation. However, the sharp increase in wave activity during the eclipse suggests a potential enhancement of AGW generation or modification due to the rapid atmospheric cooling and heating caused by the eclipse shadow.

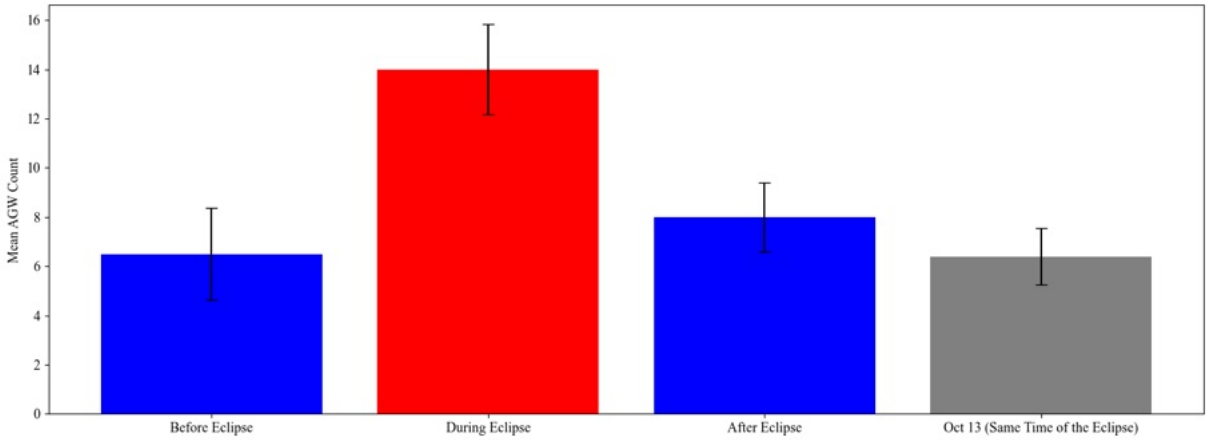

Figure 6
Mean AGW counts observed before, during, and after the solar eclipse on October 14, compared with the same time period on October 13 (non-eclipse day). Error bars represent the standard deviation of AGW counts for each period. The mean AGW count during the eclipse is significantly higher compared to other periods, indicating potential enhancement of AGW activity due to the eclipse.

Figure 6 presents a bar plot comparing the mean atmospheric gravity wave (AGW) counts across four distinct time periods: before the eclipse, during the eclipse, after the eclipse, and the same time window on October 13, a non-eclipse day. The red bar highlights the period during the eclipse, where AGW counts reached their highest mean value (14.1 ± 1.20), significantly exceeding the counts observed before the eclipse (6.5 ± 1.87) and after the eclipse (8 ± 1.41). The AGW count during the same time interval on October 13 remained comparable to the pre-eclipse period (6.4 ± 1.14), suggesting that the increased AGW activity observed during the eclipse was not a typical daily fluctuation. The error bars represent the standard deviation of AGW counts within each period.

3.1 Overall trends

In Figure 7 we show six scatter plots that illustrate the relationships between wave period and various properties of AGWs. Each subplot compares all detected AGWs (red dots) with annular eclipse AGWs (black stars), and include a linear fit (black line) to highlight any trends. Top left panel of Figure 7, shows a positive correlation between horizontal phase speed and wave period, as indicated by the positive slope. The annular

eclipse AGWs generally follow the same trend as all waves, suggesting that their horizontal phase speeds increase slightly with longer wave periods. There is a slightly negative correlation to vertical phase speeds, suggesting a slight decrease in vertical phase speed as the wave period increases. However, the magnitude of the horizontal phase speed is larger than the vertical phase speed by a factor of 10, suggesting that AGWs propagate more efficiently in the horizontal direction. The similarity in trends between annular eclipse-driven AGWs and all AGWs suggests that the presence of an eclipse does not significantly alter the fundamental propagation characteristics of these waves.

The zonal and meridional fluxes show no particular trend when compared to the wave period (middle-panels of Figure 7). This could indicate that there is no net transport of momentum in these horizontal directions. This could imply a symmetry in the wave propagation, where any momentum transported in one direction is balanced by an equal amount in the opposite direction. When both meridional and zonal momentum fluxes are zero, it implies that the waves are not exerting a significant force on the mean flow in the horizontal plane and that AGWs are not contributing to changes in the horizontal wind patterns or influencing the large-scale atmospheric circulation.

Lastly, we compare the horizontal and vertical group velocities and observe a positive correlation with the wave period, with the horizontal group velocity being a factor of 10 larger than the vertical group velocity. This confirms that the AGWs detected are propagating horizontally rather than vertically. All the plots from Figure 7 indicate that the contribution of AGWs to the atmosphere was relatively stable during the eclipse, minimizing vertical disturbances.

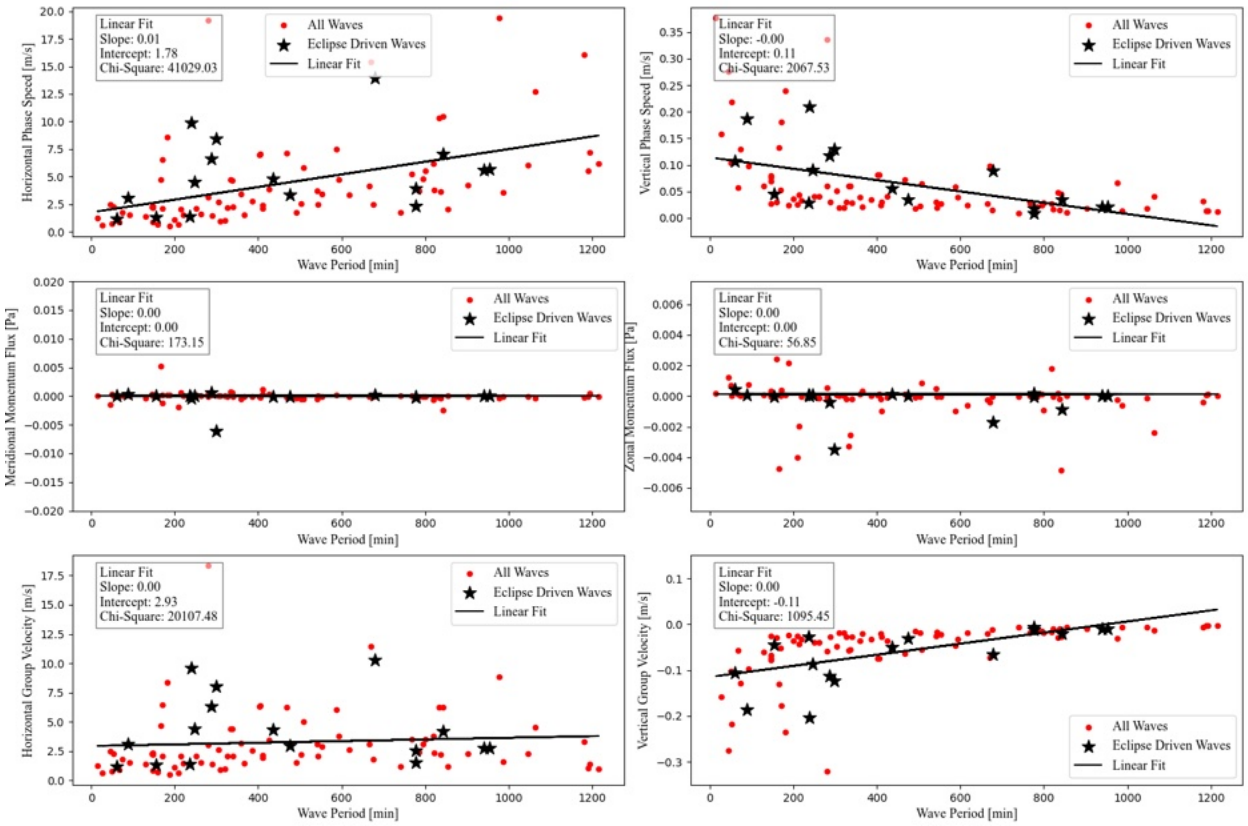

Figure 7

Scatter plots of various atmospheric gravity wave (AGW) properties versus wave period. Each subplot compares all detected waves (red dots) with annular eclipse AGWs(black stars). Linear fits (black lines) are included with corresponding slope, intercept, and chi-square values indicated in the legend boxes. Top panel shows trend in horizontal and vertical phase speed, middle panel shows trend in meridional and zonal fluxes and bottom panels show trend in horizontal and vertical group velocities.

Figure 8 in the manuscript illustrates the relationship between the horizontal and vertical wavelengths of atmospheric gravity waves (AGWs) detected during the annular solar eclipse event. This figure provides critical insights into the behavior of AGWs under stable atmospheric conditions. Stable atmospheric conditions imply that vertical motions, such as updrafts and downdrafts, are suppressed. This suppression is evident in the data presented in Figure 6, where the vertical wavelengths of the detected AGWs are much smaller than their horizontal wavelengths. In simpler terms, the waves are stretched out horizontally and compressed vertically. Furthermore, Figure 8, agrees with Figure 7, where we find small vertical wavelengths suggesting that the energy of the AGWs is confined to narrow vertical layers. This confinement is typical in a stable atmosphere, where the stratification (layering) of the atmosphere acts to inhibit vertical mixing. The presence of these smaller vertical wavelengths aligns with the expectation that AGWs, when generated in a stable atmosphere, will predominantly propagate horizontally rather than vertically (Fritts & Alexander, 2003; Holton, 1983). The horizontal wavelengths shown in Figure 8 are considerably larger compared to the vertical wavelengths. This disparity further reinforces the idea of stable atmospheric conditions, as it indicates that the waves can travel

long distances horizontally without significant vertical displacement. In a stable atmosphere, the buoyancy forces that generate AGWs may be balanced by the stratification, allowing the waves to maintain their horizontal structure longer (Holton, 1983; Fritts & Alexander, 2003).

3.2 Energy dynamics

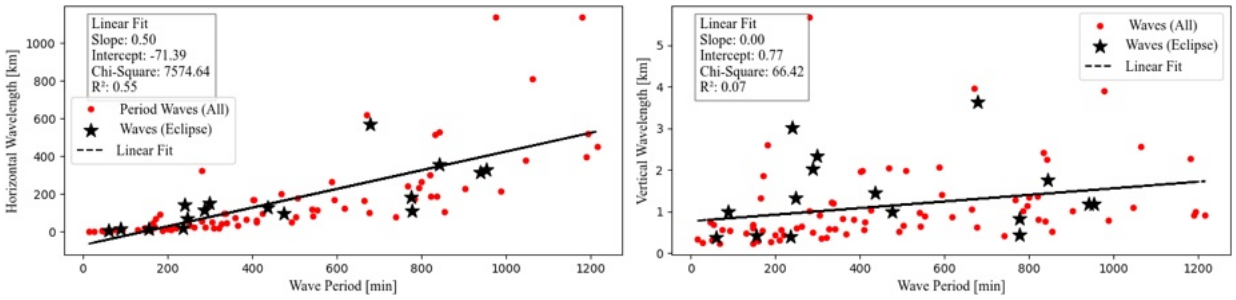

Figure 8

Wavelength compared with wave period. Left column shows relationship between Horizontal wavelength (km) and wave period (mins), for all waves (top panel). Right column shows similar relationship between vertical wavelength (km) and wave period (mins). “All Waves" represented by red dots and potentially "Eclipse Driven Waves" are represented by black crosses.

Figure 9 shows three subplots depicting the total energy, kinetic energy, and potential energy of waves as a function of detection height (in km). The first panel shows the total energy of the AGWs as a function of detection height. The total energy values vary widely, ranging from near zero to over 17.5 m^2/s^2. Annular eclipse AGWs are generally clustered around lower total energy values but are interspersed among the general population of waves (Aplin & Harrison, 2003). The majority of the waves have total energy below 5 ergs, with a few outliers reaching higher energy levels. There appears to be no clear trend indicating a significant increase or decrease in total energy with height for either all waves or annular eclipse AGWs, suggesting a consistent energy distribution across different altitudes. The second panel illustrates the kinetic energy of the AGWs relative to detection height. The kinetic energy values range from zero to over 6 ergs, with most waves exhibiting kinetic energy below 2 ergs. The distribution of annular eclipse AGWs closely follows the general distribution of all waves, indicating that the kinetic energy characteristics of annular eclipse-driven AGWs are similar to other detected waves. Although there are a few outliers with higher kinetic energy, these are not uniquely associated with the annular eclipse AGWs, further emphasizing the similarity in energy properties between annular eclipse-driven and other AGWs. The third panel presents the potential energy of the AGWs as a function of detection height. Similar to the other energy types, potential energy values range from near zero to over 15 ergs, with the majority of waves having potential energy below 5 ergs. The annular eclipse AGWs are distributed among all detected waves, with no distinct separation or clustering. This indicates that the potential energy of annular eclipse AGWs is comparable to the general wave population. A notable outlier with potential energy above 15 ergs is present but does not significantly alter the overall distribution trend.

The observation that the system's total energy is dominated by potential energy suggests a more stable atmospheric condition. This dominance indicates that the waves are more associated with horizontal displacements rather than vertical motions, which is typical in a stable atmosphere where buoyancy forces play a significant role in wave dynamics. This stability aligns with the characteristics of AGWs observed during the solar eclipse, as their energy properties do not deviate significantly from the typical behavior of AGWs driven by other atmospheric phenomena.

4. Conclusion and Future

In this manuscript, we show AGWs detected at ASC on the day of the annular eclipse, which was 14 October 2023. ASC is a topographically and population-wise isolated region in NM. We use analytical techniques from Colligan et al. (2020) to analyze these AGWs. AGWs are detected by first filtering out the first order perturbations and secondly identifying AGWs in wavelet diagrams. We represent observations of 55 AGWs on the day of the annular eclipse; 17 AGWs were observed during the eclipse which started at 14:00 UTC, with the first contact.

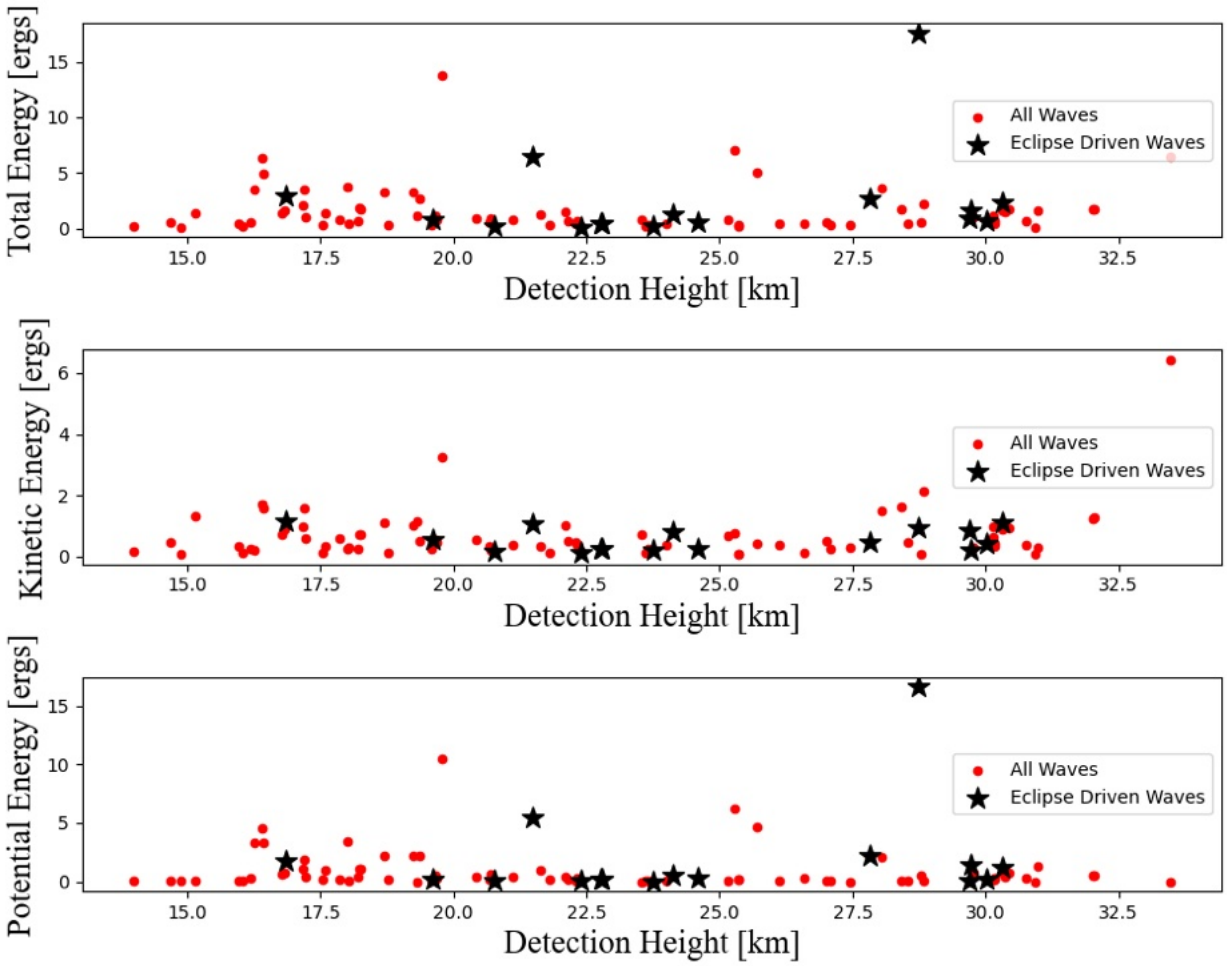

Figure 9
Energy relationship of AGWs with respect to detection height. Left panel shows total energy, which is the sum of kinetic energy (middle panel) and potential energy (right panel). “All AGWs" represented by blue dots and "Eclipse Driven AGWs” represented by red crosses.

The wavelet power spectrum results and the mapped AGW locations in Figure 3 illustrate that these waves exhibit some degree of organized propagation, though their exact origin remains uncertain. The wavelet power spectrum results and the mapped AGW locations in Figure 3 illustrate that these waves exhibit some degree of organized propagation, though their exact origin remains uncertain. While Figure 3 provides a detailed view of AGW detections and their directional propagation, Figure 4 serves as a summary, consolidating these detections to offer a broader perspective on AGW activity.

The results demonstrate that the annular solar eclipse can significantly influence AGW activity along the annularity path at ASC. AGWs were observed to propagate in various directions, as illustrated in the left panel of Figure 5 Their directional distribution appeared non-uniform, likely influenced by local topography and atmospheric conditions. However, AGWs identified during the eclipse duration were observed to follow the direction influenced by the annular eclipse’s umbral shadow. In the right panel of Figure 5, a total of 55 AGWs

were observed, with higher AGW activity detected during the eclipse period, as indicated by the red histogram bars. Figure 6 further emphasizes this finding, showing that the mean AGW count during the eclipse (14 ± 1.83) was significantly higher than during the periods before (6.5 ± 1.87) and after (8 ± 1.41) the eclipse, as well as during the same time interval on October 13 (6.4 ± 1.14). These results suggest that the eclipse can act as a driver of enhanced AGW activity.

The wave propagation direction plot shows a clear pattern, with waves emanating from the launch sites and spreading in various directions. This distribution suggests that the launch events at ASC have a widespread impact on the propagation of AGWs across the region. The histogram depicting the number of AGWs detected during different launches highlights that certain launches, particularly those during eclipses, result in a higher detection of waves.

Furthermore, the analysis of AGWs detected at ASC, as illustrated by the provided Figure 7, Figure 8, and Figure 9, highlights several key characteristics and behaviors of these waves. The comparison between annular eclipse-driven AGWs and other AGWs indicates that there is no significant difference in their energy distribution, propagation direction, amplitude, frequency, or momentum flux. This may suggest that annular eclipse events do not notably alter the fundamental properties of AGWs, and the waves detected during eclipses behave similarly to those detected under regular atmospheric conditions.

Figure 7 highlights the stable nature of the AGWs observed during the annular solar eclipse. The similarity in properties between annular eclipse AGWs and the general wave population further suggests that the eclipse event does not dramatically change the behavior of AGWs. This analysis reinforces the understanding that solar eclipses while creating unique atmospheric conditions, might not necessarily lead to substantial alterations in the fundamental dynamics of atmospheric gravity waves.

Figure 8 in our manuscript shows that the horizontal wavelengths of AGWs detected during the annular solar eclipse are significantly larger than their vertical wavelengths, indicating stable atmospheric conditions. This suggests that the waves are stretched horizontally and compressed vertically, with energy confined to narrow vertical layers, which is typical in a stable atmosphere. These findings, as shown in Figure 6, suggest that AGWs predominantly propagate horizontally under stable conditions, allowing them to travel long distances with minimal vertical displacement.

Table 1

Summary of properties of AGWs observed in different phenomena

Phenomena	Mean Horizontal Wavelength	Mean Vertical Wavelength	Mean Wave Period (m)	Mean Amplitude	Reference

Solar Eclipse	217.0	10.79	122.9	1.48	Colligan et al., 2020; Aplin & Harrison, 2003
Orographic	170.5	8.25	109.8	1.24	Smith, 1989
Convective	320.5	13.25	139.8	1.74	Lane et al., 2001
Jetstream	270.5	12.25	129.8	1.54	Sharman et al., 2012
Current manuscript	170 - 270	11.25 - 12.25	125 - 145	1.55 - 1.74	

Figure 8 demonstrates that the AGWs detected during the solar eclipse exhibit a broad range of energy values (total, kinetic, and potential) across different detection heights. The energy characteristics of annular eclipse AGWs are interspersed among the general population of detected waves, indicating that the solar eclipse generates AGWs with energy properties similar to those of AGWs driven by other atmospheric phenomena. There is no distinct trend in the energy distribution with height, and the annular eclipse AGWs do not show unique energy characteristics that set them apart from other detected waves. This suggests that while the solar eclipse induces AGWs, their energy properties are consistent with typical AGW behavior observed in the atmosphere.

A subtle change in atmospheric conditions created by an eclipse could produce AGWs that create a disturbance in the atmosphere (Colligan et al., 2020; Aplin & Harrison, 2003), such subtle changes are also seen to produce AGWs in other situations (Lane et al., 2001; Smith, 1989, Sharman et al., 2012). In Table 1, we summarize properties of some AGWs that are orographic, convective, and jet stream driven. Our finding of AGWs lies in the range of solar eclipse-driven AGWs. The horizontal wavelengths of these AGWs reported in the current manuscript range between 150 km to 270 km, which lies in the range of AGWs reported in Table 1. Our launch site was within a 200 km radius of Sacramento mountains, which implies that AGWs detected at ASC could be triggered by those mountains. We need further analysis to study the confirmed presence of eclipse-driven waves as well as study their properties. The presence of outliers in the energy and momentum flux plots indicates that there may be sporadic events or conditions that are not well understood or controlled within the study framework.

In conclusion, while this study offers significant insights into the behavior and characteristics of annular eclipse-induced AGWs at the ASC, further research is needed to address the limitations of the current analysis. Expanding the dataset, incorporating higher-resolution measurements, and exploring a broader range of detection heights would provide a deeper understanding of the dynamics and impacts of these waves. Such

advancements would enable a more detailed and accurate assessment of AGWs and their interaction with atmospheric and environmental factors. In a follow-up manuscript, we plan to focus on AGWs generated by total solar eclipses, examining their properties in greater detail to complement the findings of this study.

Acknowledgments

We would like to thank NSF grant #1936336. O.V. also acknowledges funding from the New Mexico Space Grant Scholarship and Fellowship Program. The funding for the New Mexico Space. Grant Scholarship and Fellowship Program is contained in the National Aeronautics and Space Administration (NASA) Cooperative Agreement 80NSSC20M0034. And Nationwide Eclipse Ballooning Project (NEBP) that funded travel and logistics of the eclipse travel. We acknowledge the cooperation of the Artesia Science Centre staff.

References

1. Espenak, F., & Anderson, J. (2007). *Total solar eclipse of 2008 August 01* (NASA/TP-2007-214149). National Aeronautics and Space Administration, Goddard Space Flight Center. Retrieved from https://eclipse.gsfc.nasa.gov/SEpubs/20080801/rp.html ↩
2. Pasachoff, J. M. (2009). Solar eclipses as an astrophysical laboratory. *Nature*, *459*(7248), 789-795. https://doi.org/10.1038/nature07987 ↩
3. Fritts, D. C., & Alexander, M. J. (2003). Gravity wave dynamics and effects in the middle atmosphere. *Reviews of geophysics*, *41*(1). https://doi.org/10.1029/2001RG000106 ↩
4. Colligan, T., Fowler, J., Godfrey, J., & Spangrude, C. (2020). Detection of stratospheric gravity waves induced by the total solar eclipse of July 2, 2019. *Scientific reports*, *10*(1), 19428. https://doi.org/10.1038/s41598-020-75098-2 ↩
5. Vadas, S. L., & Liu, H. L. (2009). Generation of large-scale gravity waves and neutral winds in the thermosphere from the dissipation of convectively generated gravity waves. *Journal of Geophysical Research: Space Physics*, *114*(A10). https://doi.org/10.1029/2009JA014108 ↩
6. Holton, J. R. (1983). The influence of gravity wave breaking on the general circulation of the middle atmosphere. *Journal of Atmospheric Sciences*, *40*(10), 24. https://doi.org/10.1175/1520-0469 ↩
7. Aplin, K. L., & Harrison, R. G. (2003). Meteorological effects of the eclipse of 11 August 1999 in cloudy and clear conditions. *Proceedings of the Royal Society of London. Series A: Mathematical, Physical and Engineering Sciences*, *459*(2030), 353-371. https://doi.org/10.1098/rspa.2002.1042 ↩
8. Zerefos, C. S., Gerasopoulos, E., Tsagouri, I., Psiloglou, B. E., Belehaki, A., Herekakis, T., ... & Mihalopoulos, N. (2007). Evidence of gravity waves into the atmosphere during the March 2006 total solar eclipse. *Atmospheric Chemistry and Physics*, *7*(18), 4943-4951. https://doi.org/10.5194/acp-7-4943-2007 ↩

9. Liu, H. L., & Roble, R. G. (2002). A study of a self-generated stratospheric sudden warming and its mesospheric–lower thermospheric impacts using the coupled TIME-GCM/CCM3. *Journal of Geophysical Research: Atmospheres*, *107*(D23), ACL-15. http://dx.doi.org/10.1029/2001JD001533 ↩
10. Goodwin, G. L., & Hobson, G. J. (1978). Atmospheric gravity waves generated during a solar eclipse. *Nature*, *275*(5676), 109-111. https://doi.org/10.1038/275109a0 ↩
11. Qiu, L., Yamazaki, Y., Yu, T., Becker, E., Miyoshi, Y., Qi, Y., ... & Liu, H. (2023). Numerical simulations of metallic ion density perturbations in sporadic E layers caused by gravity waves. *Earth and Space Science*, *10*(8), e2023EA003030. https://doi.org/10.5194/egusphere-egu23-6372 ↩
12. Torrence, C., & Compo, G. P. (1998). A practical guide to wavelet analysis. *Bulletin of the American Meteorological society*, *79*(1), 61-78. https://doi.org/10.1175/1520-0477(1998)079<0061:APGTWA>2.0.CO;2 ↩
13. Zink, F., & Vincent, R. A. (2001). Wavelet analysis of stratospheric gravity wave packets over Macquarie Island: 1. Wave parameters. *Journal of Geophysical Research: Atmospheres*, *106*(D10), 10275-10288. https://doi.org/10.1029/2000JD900847 ↩
14. Moffat-Griffin, T., Hibbins, R. E., Jarvis, M. J., & Colwell, S. R. (2011). Seasonal variations of gravity wave activity in the lower stratosphere over an Antarctic Peninsula station. *Journal of Geophysical Research: Atmospheres*, *116*(D14). https://doi.org/10.1029/2010JD015349 ↩
15. Pfenninger, M., Liu, A. Z., Papen, G. C., & Gardner, C. S. (1999). Gravity wave characteristics in the lower atmosphere at South Pole. *Journal of Geophysical Research: Atmospheres*, *104*(D6), 5963-5984. https://doi.org/10.1029/98JD02705 ↩
16. Ren, D., Lei, J., Liu, H. L., Wang, W., Yue, J., & Liu, H. (2023). Influence of mesospheric gravity wave drag on the formation of winter helium bulge in the thermosphere. *Journal of Geophysical Research: Space Physics*, *128*(2), e2022JA031022. https://doi.org/10.1029/2022JA031022 ↩
17. Murphy, D. J., Alexander, S. P., Klekociuk, A. R., Love, P. T., & Vincent, R. A. (2014). Radiosonde observations of gravity waves in the lower stratosphere over Davis, Antarctica. *Journal of Geophysical Research: Atmospheres*, *119*(21), 11-973. https://doi.org/10.1002/2014JD022448 ↩
18. Koushik, N., Kumar, K. K., Subrahmanyam, K. V., Ramkumar, G., Girach, I. A., Santosh, M., ... & Shreedevi, P. R. (2019). Characterization of inertia gravity waves and associated dynamics in the lower stratosphere over the Indian Antarctic Station, Bharati (69.4 S, 76.2 E) during Austral summers. *Climate Dynamics*, *53*, 2887-2903. https://doi.org/10.1007/s00382-019-04665-9 ↩

19. Yoo, J. H., Song, I. S., Chun, H. Y., & Song, B. G. (2020). Inertia-Gravity Waves Revealed in Radiosonde Data at Jang Bogo Station, Antarctica (74 degrees 37'S, 164 degrees 13'E): 2. Potential Sources and Their Relation to Inertia-Gravity Waves. *Journal of Geophysical Research- Atmospheres*, *125*(7). https://doi.org/10.1029/2019JD032260 ↩

20. Smith, R. B. (1989). Hydrostatic airflow over mountains. In *Advances in geophysics* (Vol. 31, pp. 1-41). Elsevier. ↩

21. Lane, T. P., Reeder, M. J., & Clark, T. L. (2001). Numerical modeling of gravity wave generation by deep tropical convection. *Journal of the Atmospheric Sciences*, *58*(10), 1249-1274. https://doi.org/10.1175/1520-0469 ↩

22. Sharman, R. D., Trier, S. B., Lane, T. P., & Doyle, J. D. (2012). Sources and dynamics of turbulence in the upper troposphere and lower stratosphere: A review. *Geophysical Research Letters*, *39*(12). https://doi.org/10.1029/2012GL051996 ↩